Mesoscale Predictability of an Extreme Warm-Season Precipitation Event

FUQING ZHANG, ANDREW M. ODINS, AND JOHN W. NIELSEN-GAMMON

Department of Atmospheric Sciences, Texas A&M University, College Station, Texas

(Manuscript received 22 November 2004, in final form 28 August 2005)

ABSTRACT

A mesoscale model is used to investigate the mesoscale predictability of an extreme precipitation event over central Texas on 29 June 2002 that lasted through 7 July 2002. Both the intrinsic and practical aspects of warm-season predictability, especially quantitative precipitation forecasts up to 36 h, were explored through experiments with various grid resolutions, initial and boundary conditions, physics parameterization schemes, and the addition of small-scale, small-amplitude random initial errors. It is found that the high-resolution convective-resolving simulations (with grid spacing down to 3.3 km) do not produce the best simulation or forecast. It was also found that both the realistic initial condition uncertainty and model errors can result in large forecast errors for this warm-season flooding event. Thus, practically, there is room to gain higher forecast accuracy through improving the initial analysis with better data assimilation techniques or enhanced observations, and through improving the forecast model with better-resolved or -parameterized physical processes. However, even if a perfect forecast model is used, small-scale, small-amplitude initial errors, such as those in the form of undetectable random noise, can grow rapidly and subsequently contaminate the short-term deterministic mesoscale forecast within 36 h. This rapid error growth is caused by moist convection. The limited deterministic predictability of such a heavy precipitation event, both practically and intrinsically, illustrates the need for probabilistic forecasts at the mesoscales.

1. Introduction

The study of atmospheric predictability began with Thompson (1957) and Lorenz (1963, 1969). With the ever-improving performance of numerical prediction models and ever-increasing computational resources, recently there is a renewed interest in the predictability of the daily weather, especially at the mesoscale (e.g., Ehrendorfer 1997; Errico et al. 2002). Broadly speaking, predictability can have two fundamentally different meanings. *Intrinsic predictability* can be defined as "the extent to which prediction is possible if an optimum procedure is used" in the presence of infinitesimal initial errors (Lorenz 1969). *Practical predictability*, on the other hand, can be specified as the ability to predict based on the procedures that are currently available. Practical predictability is limited by realistic uncertainties in both the initial states and the forecast models, which in general are not infinitesimally small (Lorenz 1996).

Corresponding author address: Dr. Fuqing Zhang, Dept. of Atmospheric Sciences, Texas A&M University, 3150 TAMU, College Station, TX 77843-3150.
E-mail: fzhang@tamu.edu

Both the intrinsic and practical aspects of mesoscale predictability of the "surprise" snowstorm of January 2000 were explored in recent papers (Zhang et al. 2002, 2003, hereafter referred to as ZSR02, ZSR03; Zhang 2005). In ZSR02, various experiments suggested that insufficient model grid resolution and large uncertainties in the initial conditions (judging from the discrepancy among the analyses from different operational centers) both contributed significantly to problems in the forecast. Further experiments in both ZSR02 and ZSR03 demonstrated the possible influence of initial errors of small amplitude and scale on the numerical prediction of this event. Because of the chaotic nature of the atmosphere, the small initial errors in the forecast model grew rapidly at small scales, quickly saturated, and then spread upscale, substantially contaminating the 1–2-day mesoscale forecast. Rapid upscale error growth was dependent on moist convection. Similar error growth characteristics and dependence upon moist convection has recently been identified in idealized baroclinic waves amplifying in a conditionally unstable atmosphere (Tan et al. 2004).

The aforementioned mesoscale predictability studies were focusing primarily on midlatitude weather systems

with strong baroclinicity. How much more or less predictable are warm-season and/or subtropical systems, including mesoscale convective systems (MCSs), which usually possess strong conditional instability but weak baroclinicity? In practice, warm-season weather, especially precipitation, remains the least accurate forecast element at all scales (e.g., Olson et al. 1995). It is uncertain whether this critical forecasting problem is one of highly chaotic atmospheric behavior and, therefore, inherent (intrinsic) unpredictability, or one of initial condition or model uncertainty (practical), which might therefore be solved through further model development, enhancing observation system deployment, or advances in data assimilation. Islam et al. (1993) and Snyder and Zhang (2003) demonstrated that errors grow very rapidly at convective scale in the weakly forced, warm-season environment. However, an earlier study by Reynolds et al. (1994) found that, under a perfect model assumption, the error growth rate due to initial condition error in the Tropics is several times smaller than in midlatitudes, even while the error growth rate due to model deficiencies is considerably larger. A recent study by Carbone et al. (2002) also showed significance persistence (1–3 days) of warm-season convective precipitation systems derived from composite radar analyses. This, in principle, would imply that these warm-season convective systems could have a much longer predictable time scale. During the Bow Echo and Mesoscale Convective Vortex Experiment (BAMEX) over the central United States in summer 2003, the Weather Research and Forecast (WRF) model was used to provide real-time forecasts to aid the planning of operations. Done et al. (2004) suggest that this high-resolution weather forecast model was able to correctly capture the timing, location, and mode of MCSs in the majority of BAMEX cases, although the verification criteria they used to match the forecasted MCSs to the observed ones are rather flexible, which may not satisfy all users.

Despite these and other studies that examine various factors that affect the prediction of warm-season precipitation, the error dynamics that limit the predictability of the warm-season convective systems and the difference between those of the midlatitude baroclinic weather systems remain largely unknown. Understanding the limit of mesoscale predictability and the associated error growth dynamics is essential for setting up expectations and priorities for advancing deterministic mesoscale forecasting and for providing guidance on the design, implementation, and application of short-range ensemble prediction systems (e.g., Tracton and Kalnay 1993; Ehrendorfer 1997; Stensrud et al. 1999; Errico et al. 2002).

A heavy rainfall event began over central Texas on 29 June 2002 and lasted through 7 July 2002. The heaviest precipitation fell near San Antonio, Texas, but several counties in the area received large amounts of precipitation, causing flooding, millions of dollars in damages, and loss of life. Operational models used at the National Centers for Environmental Prediction (NCEP) had forecasted some heavy precipitation in the area; however, the timing, duration, and intensity of heavy precipitation were not well forecasted in real time. The current study explores both the intrinsic and practical aspects of the warm-season predictability of the San Antonio flooding event. Experiments with grid spacing down to 3.3 km will also be used to assess the impact of resolution on forecast accuracy. Through this case study, we will seek to identify the fundamental processes controlling the error growth dynamics and predictability of warm-season mesoscale weather leading to severe flooding.

An overview of the flooding event will be presented in section 2. The model and experimental design will be described in section 3. Practical and intrinsic predictability of this event will be considered in sections 4 and 5, respectively. Section 6 contains the concluding remarks including discussions on the different error growth characteristics between this warm-season event and the January 2000 snowstorm.

2. Overview of the flooding event

Beginning early on 29 June 2002, and lasting through 7 July 2002, an extreme rainfall event occurred in Texas with the heaviest precipitation falling in the south-central portion of the state centered near the city of San Antonio. The San Antonio International Airport (SAT) had an event total precipitation of 410 mm (16.16 in.) with 242 mm (9.52 in.) falling between 1200 UTC 1 July and 1200 UTC 2 July 2002. The largest event total occurred at a nearby station, Camp Verde 3 W, which recorded 868 mm (34.17 in.) of precipitation. Figure 1a shows an NCEP gridded analysis of the 8-day event total precipitation between 1200 UTC 28 June 2002 and 1200 UTC 7 July 2002 and Fig. 1b shows the 24-h accumulated precipitation valid at 1200 UTC 2 July.

Initially, widely scattered precipitation fell on 29 June, with the southern portions of the state receiving the majority of the rainfall. By 30 June, more widespread precipitation fell across the southeastern half of the state, with heavier rainfall near the Austin area. Rainfall continued in the central portion of the state, with the heaviest amounts occurring primarily in the south-central regions of the state for the next 3 days

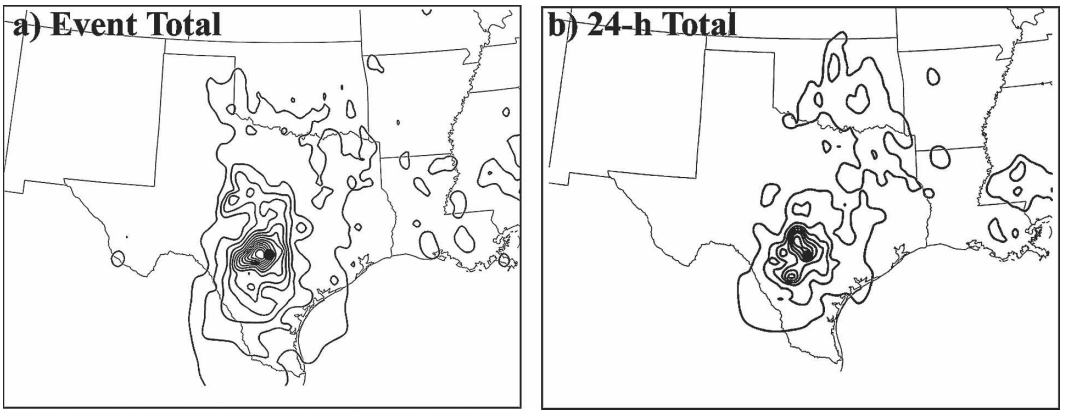

FIG. 1. The observational analysis of accumulated precipitation from gridded data acquired through NCDC. (a) The 8-day event total precipitation (every 50 mm) from 1200 UTC 28 Jun 2002 to 1200 UTC 7 Jul 2002. (b) The 24-h accumulated precipitation (every 20 mm) valid at 1200 UTC 2 Jul 2002. The location of SAT is marked with dots.

(e.g., Fig. 1b). The precipitation was slowly shifting away from the San Antonio area toward the west by 4 July, but this relief was short lived as heavier rain again fell on central Texas on 5 July. By 6 July, the system responsible for delivering the great quantity of rain had finally moved to the west of the area. With such heavy precipitation, damage was extreme. According to National Climate Data Center (NCDC), 29 counties experienced damage from flooding and were declared federal disaster areas. Rivers and streams flooded, and lake levels rose to record levels. Seven people lost their lives in floodwaters, numerous homes were destroyed and damages were estimated to be near $500 million. Although this was an extreme event, climatologically speaking such an event is not unheard of in this area (e.g., Caracena and Fritsch 1983; Nielsen-Gammon et al. 2006).

Detailed synoptic and mesoscale discussions of the event can be found in Odins (2004) and Nielsen-Gammon et al. (2006). The basic meteorological setting is shown in Figs. 2 and 3: the 500-hPa PV, geopotential heights, and wind vectors (Fig. 2), and the MSLP, relative humidity, and wind vectors at the surface (Fig. 3) at 1200 UTC of 28 June, 30 June, 2 July, and 4 July. Typical of early season extreme rainfall events in Texas (Nielsen-Gammon et al. 2006), there is a slow-moving north–south-oriented upper-level trough across central Texas throughout the event (Fig. 2) accompanied by strong low-level southeasterly flow that continuously transports humid air to the flooding region (Fig. 3). With the vertically stacked (not shown) upper-level disturbance embedded in very weak upper-level flow and weak shear, there is relatively weak synoptic forcing for this event. Smaller-scale processes, such as the lifting by the elevated topography just west of the San Antonio area, may have contributed to the localization of the event (Nielsen-Gammon et al. 2006; Caracena and Fritsch 1983).

3. Model description and experimental design

Version 3 of the fifth-generation National Center for Atmospheric Research–Pennsylvania State University (NCAR–PSU) nonhydrostatic Mesoscale Model (MM5, Dudhia 1993) was used for this study. The control 30-km resolution simulation (hereafter also referred to as CNTL30KM) employs a horizontal domain (D1) of 190 × 120 grid points with 23 vertical layers covering the entire continental United States (Fig. 4). The Mellor–Yamada PBL scheme (Mellor and Yamada 1982), Reisner microphysics scheme with graupel (Reisner et al. 1998), and the Grell cumulus parameterization scheme (Grell 1993) are used for the control experiment. CNTL3.3KM is the same as CNTL30KM but with the addition of two nested domains with 241 × 181 horizontal grid points for the 10-km resolution nested domain (D2) and 271 × 271 grid points for the 3.3-km resolution nested domain (D3). Two-way nesting is used for the lateral boundary conditions for D2 and D3. No cumulus parameterization is used for D3 [this is a common configuration of MM5 despite potential problems discussed in Warner and Hsu (2000)]. Except for experiments described in section 5c, all the simulations were initialized at 0000 UTC 1 July 2002 and integrated for 36 h. The NCEP Global Energy and Water Cycle Experiment (GEWEX) Continental-Scale International Project (GCIP) analysis (constructed from the real-time operational Eta Model analysis with 40-km resolution) is used to create both the initial and lateral

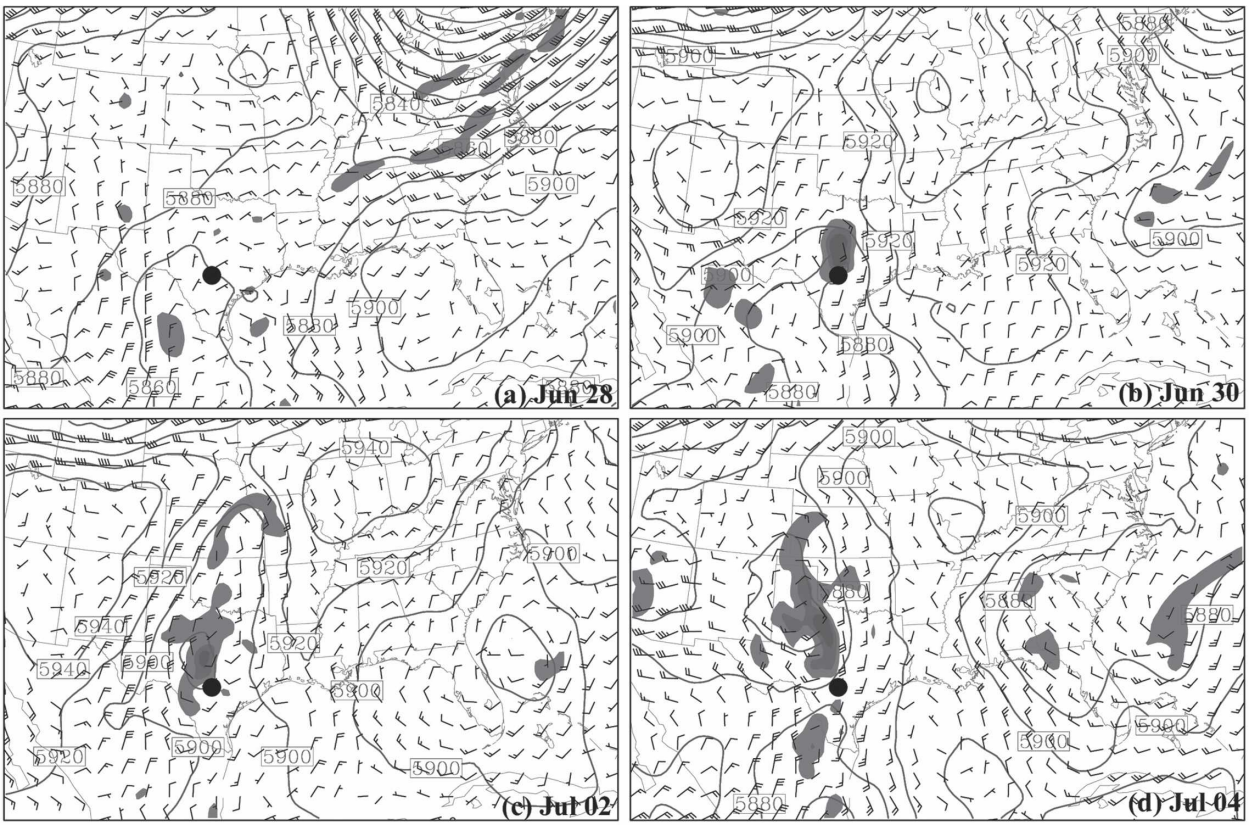

FIG. 2. The MM5 observational analysis of 500-hPa winds (full barb denotes 5 m s^{-1}), geopotential heights (solid, every 20 m), and PV (>1.0 PVU shaded, every 0.5 PVU) valid at 1200 UTC (a) 28 Jun, (b) 30 Jun, (c) 2 Jul, and (d) 4 Jul 2002.

boundary conditions. In section 5c, the pairs of control and perturbed simulations were performed for all 36-h integration periods during this multiday event (i.e., initialized every 12 h from 0000 UTC 28 June to 0000 UTC 4 July 2002).

Similar to ZSR02, a series of experiments has been designed to examine the *short-term practical predictability* of this warm-season flooding event given realistic uncertainties in the current operational forecast systems such as those in the initial states, boundary conditions, grid resolutions, and subgrid-scale parameterizations. These experiments are listed in Table 1. Also complementary to ZSR03, various experiments have been performed to examine the *mesoscale intrinsic predictability* of this event at various times during the precipitation event through the introduction of small-scale, small-amplitude perturbations in the model initial conditions. These experiments include the sensitivity of error growth to different realizations and different amplitudes of the initial random perturbations, under different physics parameterizations, at different initialization times, and with different model resolutions (detailed in section 5).

4. Practical forecast uncertainties

a. The control experiments and resolution dependence

Similar to ZSR02, two control experiments (CNTL30KM and CNTL3.3KM) with effective grid increments of 30 and 3.3 km, respectively, have been performed (refer to section 3 and Fig. 4 for the model configurations). The 24-h accumulated precipitation fields valid at 1200 UTC 2 July 2002 (with a 36-h lead time) from these control simulations are shown in Fig. 5.

Compared to the observational analysis, CNTL30KM with a 36-h lead time predicts reasonably well the intensity and location of the heavy precipitation over the San Antonio area, though the forecasted precipitation is slightly shifted to the west (Fig. 5a versus Fig. 1b). However, the CNTL3.3KM simulation missed the event completely. This is in strong contrast to the forecast sensitivity of the "surprise" snowstorm of 24–25 January 2000 examined in ZSR02, in which better resolution resulted in better representation of the moist physics and thus a better forecast. Examination of the

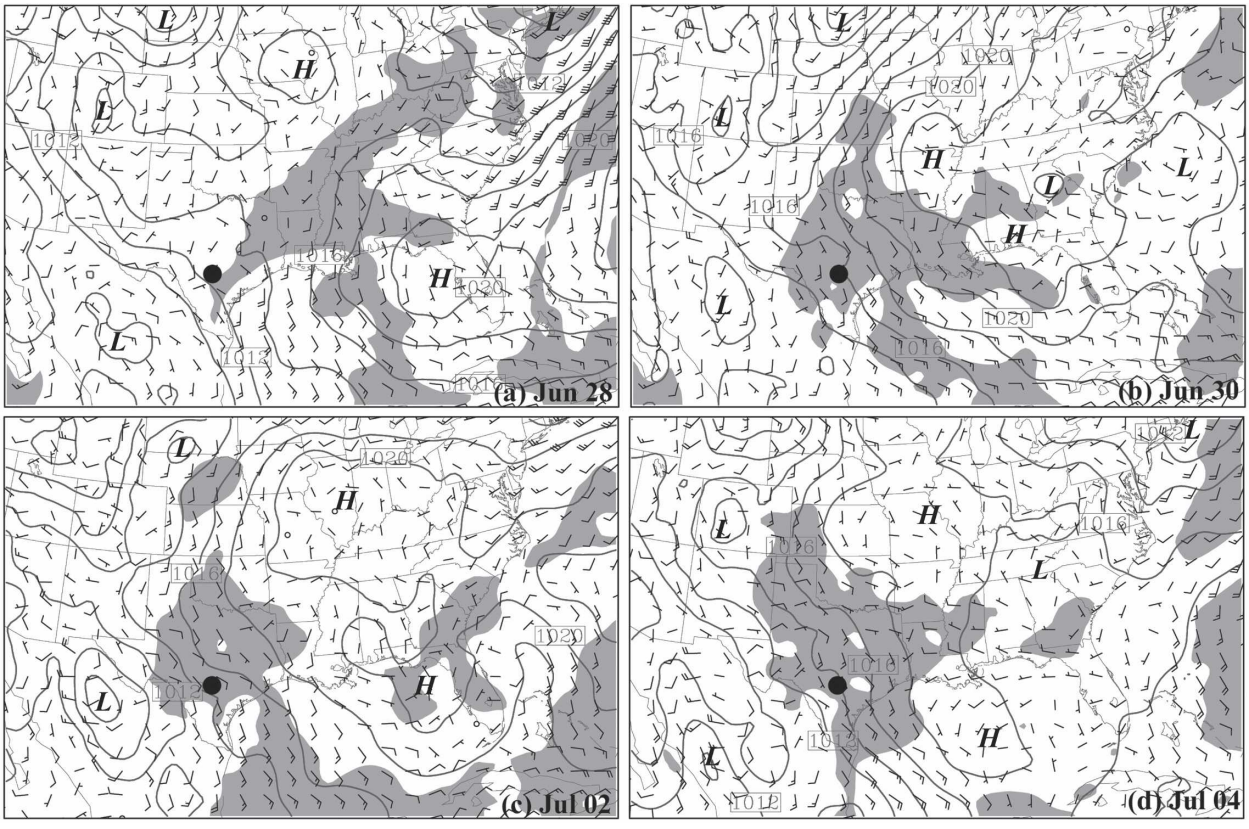

FIG. 3. The MM5 observational analysis of surface winds (full barb denotes 5 m s^{-1}), MSLP (solid, every 2 hPa), and relative humidity (>90% shaded) valid at 1200 UTC on (a) 28 Jun, (b) 30 Jun, (c) 2 Jul, and (d) 4 Jul 2002.

evolution of the 500-hPa wind difference between CNTL30KM and CNTL3.3KM shows that the difference grows most rapidly in the area of the flood event, implying lower predictability of this region (Figs. 6a and 6b).

Further examination of the time evolution of accumulated precipitation shows that the mean precipitation from the 30-km grid of CNTL30KM and CNTL3.3KM is fairly comparable throughout the simulation if averaged over domain 2 (Fig. 7a), but the mean precipitation in CNTL3.3KM is much weaker when averaged over a 300 km × 300 km area centered around the San Antonio area between 12 and 36 h (Fig. 7b). The failure of CNTL3.3KM is not likely due to insufficient vertical resolution, because similar precipitation forecasts are produced by another higher-resolution experiment (not shown) identical to CNTL3.3KM but with doubled vertical resolution. Degradations of higher-resolution forecasts were also found in Gallus (2002) who compared the performance of 30- versus 10-km grids of the Eta Model in 20 different cases. It is possible that some subgrid-scale physical parameterizations are more suitable for use in coarser resolutions in the case of weak synoptic forcing such as this event. Convective initiation in CNTL3.3KM, which relies solely on grid-scale processes, may not be sufficient since convection only becomes marginally resolvable with 3.3-km grid spacing despite many recent successes in convective resolving experiments with grid spacing of 4–6 km (e.g., Done et al. 2004; Fowle and Roebber 2003). This is different from CNTL30KM, which employs the Grell cumulus parameterization, allowing convective initiation prior to the elimination of convective inhibition (CIN). Examination of the soundings around the San Antonio area indicates that CNTL3.3KM has similar or even higher moist instability and stronger lifting than CNTL30KM (not shown) near the time of initiation of convection, though much less convection was triggered between 12 and 36 h. It is also possible that high-resolution simulations sometimes may require better initialization, if the intrinsic error growth is faster (and predictability shorter) in higher-resolution simulations (to be examined in section 5).

Unless otherwise specified, the following sensitivity experiments will be based on and compared to

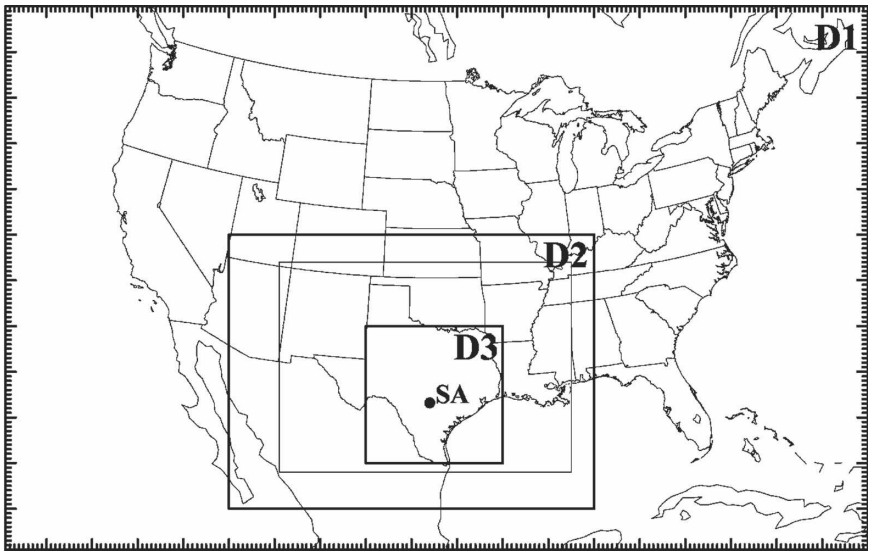

FIG. 4. The relative locations of MM5 model domains. The grid increments of domain 1 (D1), domain 2 (D2), and domain 3 (D3) are 30, 10, and 3.3 km, respectively.

CNTL30KM, which facilitates comparison with similar experiments in ZSR02.

b. Sensitivity to initial and boundary conditions

Many mesoscale models utilize the initial and boundary conditions interpolated from larger-scale (global) models, so in this section we will examine the impacts on the short-term limited-area model forecast of using different analyses as initial and boundary conditions.

The experiment NNRPic is identical to CNTL30KM except that the NCEP–NCAR reanalysis (NNRP) was used to initialize the MM5 30-km resolution simulation. Similarly, TOGAic is identical to CNTL30KM except that the European Centre for Medium-Range Weather Forecasts (ECMWF) Tropical Ocean Global Atmosphere (TOGA) analysis was used for the initial condition. The same boundary conditions as in CNTL30KM are used for NNRPic and TOGAic.

Significant differences in both intensity and locations can be found in the 24-h accumulated precipitation forecast from the simulations with different initial analyses although all three runs forecasted heavy precipitation in south-central Texas and other precipitation near the Texas–Oklahoma border (Figs. 5a, 5c, and 5d). The TOGAic run produced the greatest precipitation in the San Antonio area but it significantly overpredicted precipitation all along the Texas coast (Fig. 5d). The NNRPic run produced some intense, localized precipitation just west of San Antonio (Fig. 5c) but the areal coverage is too small compared to observations (Fig. 1b). The 500-hPa winds begin with large-scale differences between NNRPic and TOGAic (Figs. 6c and 6d) even though the difference total energy (DTE) integrated over domain 2 of Fig. 4 between simulations with different initial analyses shows relatively small error growth over the 36-h forecast integration (Fig. 8). As in ZSR03, the difference total energy or DTE is defined as

$$\mathrm{DTE} = \frac{1}{2}\sum (U'^2_{ijk} + V'^2_{ijk} + \kappa T'^2_{ijk}),$$

TABLE 1. List of the sensitivity experiments with practical forecast uncertainties. The boldface italics denote the difference betwen CNTL30KM.

Expt	Grid spacing (km)	Initial analysis	Lateral boundary	Cumulus scheme	Microphysics scheme	PBL scheme
CNTL30KM	***30***	***GCIP***	***GCIP***	***Grell***	***Reisner***	***Eta***
CNTL3.3KM	***30, 10, 3.3***	GCIP	GCIP	***None***	Reisner	Eta
NNRP30KM	30	***NNRP***	GCIP	Grell	Reisner	Eta
TOGA30KM	30	***TOGA***	GCIP	Grell	Reisner	Eta
NNRPbc	30	GCIP	***NNRP***	Grell	Reisner	Eta
TOGAbc	30	GCIP	***TOGA***	Grell	Reisner	Eta
KFcps	30	GCIP	GCIP	***KF***	Reisner	Eta
GDmps	30	GCIP	GCIP	Grell	***Goddard***	Eta
MRFpbl	30	GCIP	GCIP	Grell	Reisner	***MRF***

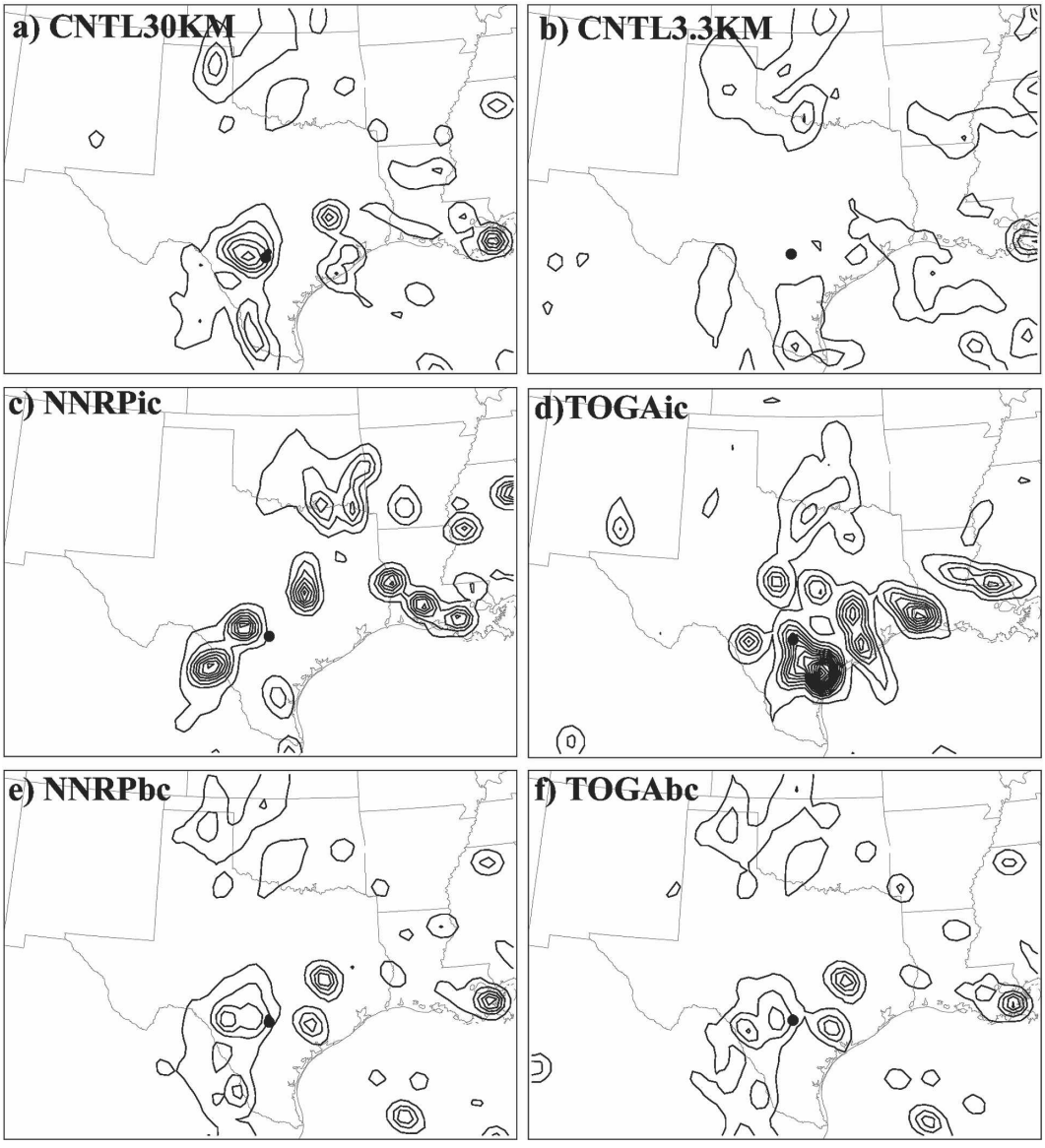

FIG. 5. The 24-h accumulated precipitation (every 20 mm) from 1200 UTC 1 Jul to 1200 UTC 2 Jul 2002 from experiments (a) CNTL30KM, (b) CNTL3.3KM, (c) NNRPic, (d) TOGAic, (e) NNRPbc, and (f) TOGAbc. All experiments started at 0000 UTC 1 Jul 2002.

where U', V', and T' are the difference wind components and difference temperature between two simulations, $\kappa = C_p/T_r$ (the reference temperature $T_r = 287$ K), and i, j, and k run over x, y, and σ grid points.

Because the difference between analyses from different operational centers represents a crude estimate of the lower bound of the realistic initial condition uncertainties in the operational NWP systems (e.g., Grimit and Mass 2002; Eckel and Mass 2005), a deterministic forecast using any one of these initial analyses would have limited (practical) predictability of this extreme flooding event. In other words, present-day errors in the initial conditions may be severely detrimental to deterministic forecasts of such extreme flooding events. Uncertainties from different initial analyses may arise from 1) insufficient or inaccurate observations, 2) imperfect data assimilation schemes, 3) poor representation of the background state, usually from previous forecasts, and 4) interpolations to regional-scale models.

Boundary condition uncertainties may also be an important source of errors for limited-area forecasts (Warner et al. 1997; Laprise et al. 2000). NNRPbc and TOGAbc are identical to CNTL30KM except that the

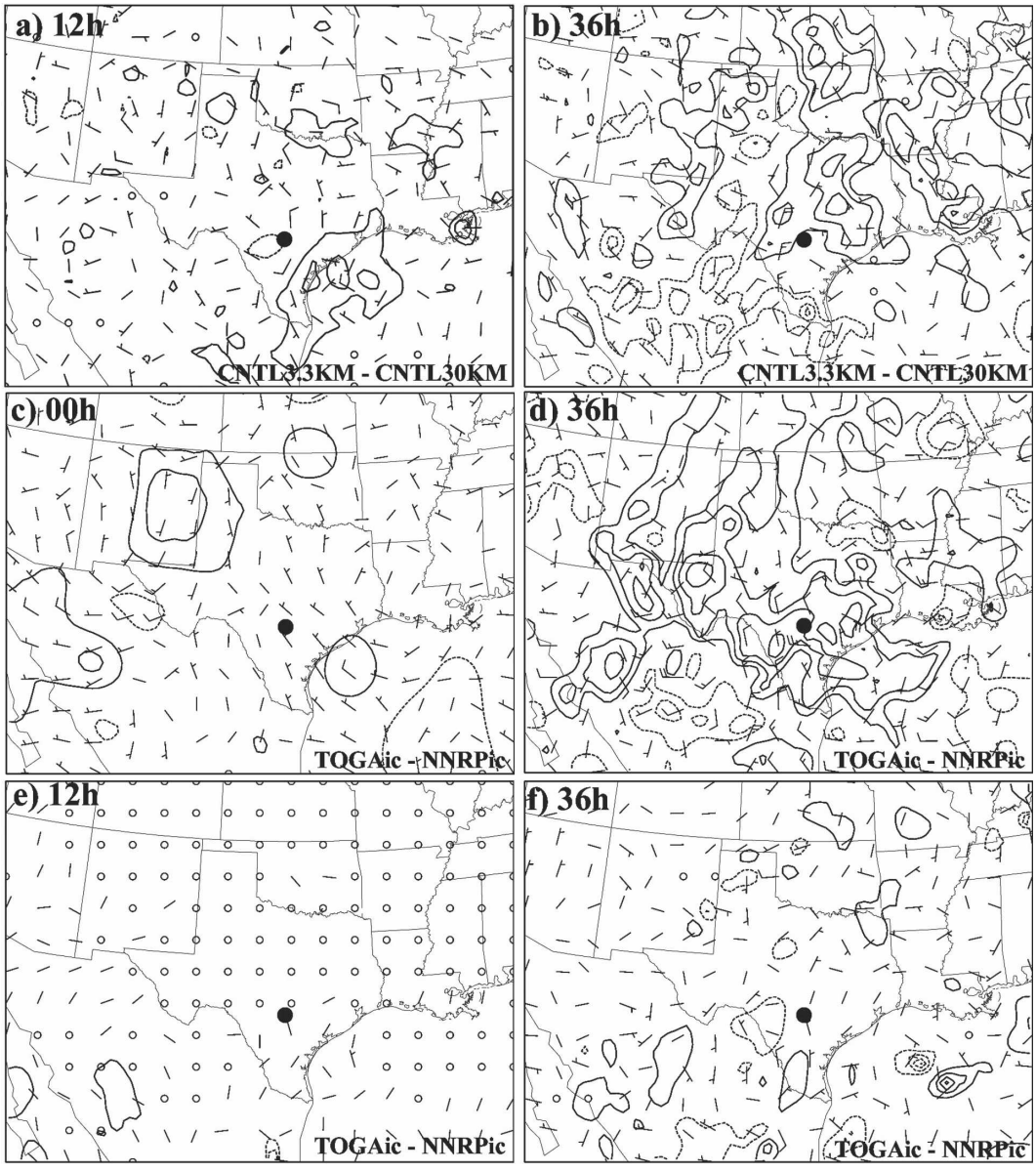

FIG. 6. The 500-hPa temperature (every 0.5 K; dashed, negative; solid, positive) and wind vectors (full barb, 5 m s^{-1}) difference between CNTL30KM and CNTL3.3KM valid at (a) 12- and (b) 36-h forecast times, between NNRPic and TOGAic valid at (c) 0- and (d) 36-h forecast times, and between NNRPbc and TOGAbc valid at (e) 12- and (f) 36-h forecast times. All experiments started at 0000 UTC 1 Jul 2002.

NCEP–NCAR reanalysis and the ECMWF TOGA analysis were used to provide the boundary conditions. However, because the primary region of interest (heavy precipitation in the San Antonio area) is far away from the lateral boundaries, TOGAbc and NNRPbc show no significant differences in the precipitation forecast (Figs. 5e and 5f) compared to CNTL30KM, except that both have a noticeable reduction in precipitation intensity. The 500-hPa wind and temperature differences are also significantly smaller than those found when using different initial analyses (Figs. 6e and 6f). The domain-integrated DTE between TOGAbc and NNRPbc is less than 30% of that between TOGAic and NNRPic through the 36-h forecast time (Fig. 8).

c. Sensitivity to model physics parameterizations

Another source of prediction error is the forecast model itself. Model error is possibly one of the least understood aspects of numerical weather prediction models (e.g., Hansen 2002; Zupanski et al. 2002).

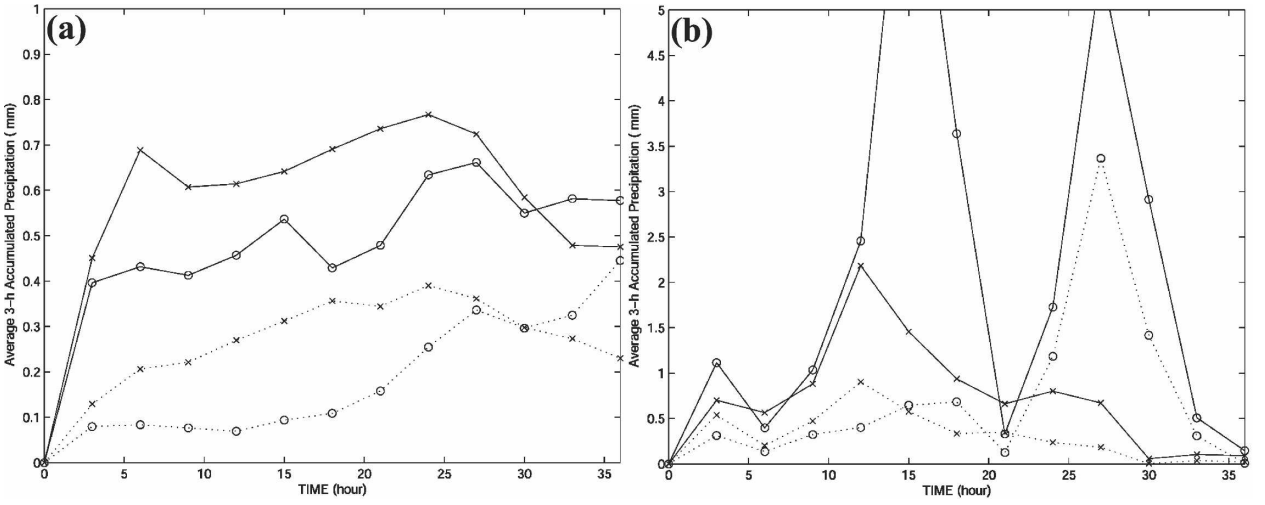

FIG. 7. (a) Time evolution of mean 3-h accumulated precipitation (mm) in the 30-km grid of CNTL30KM (solid with circles) and CNTL3.3KM (solid with times signs), as well as mean absolute difference between CNTL30KM and PERT30KM (dotted with circles) and between CNTL3.3KM and PERT3.3KM (dotted with times signs) averaged over the D2 area (refer to Fig. 4). (b) As in (a) except for averaged over a 300 km × 300 km area surrounding the San Antonio region.

Among different sources of model errors, parameterizations of subgrid-scale physical processes, which fundamentally are used to solve unclosed equation sets, are believed to be the most significant. Forecast sensitivity to nine different combinations of convective, microphysical, and boundary layer parameterization schemes was examined in Nielsen-Gammon et al. (2006) and was found to be large. Three such experiments are reproduced here for completeness.

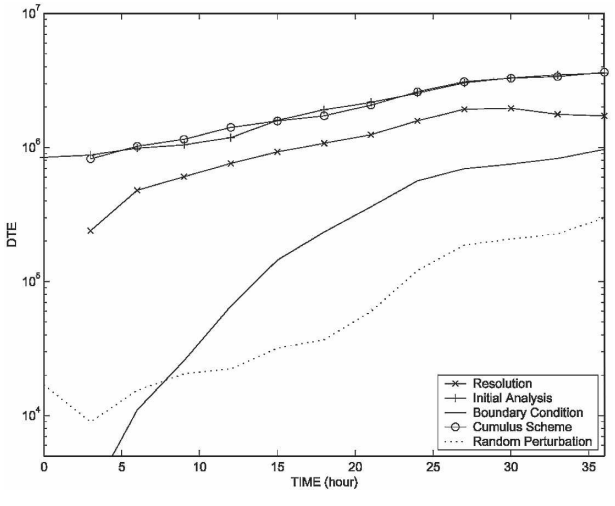

FIG. 8. Evolution of difference total energy (DTE, $m^2 s^{-2}$) between experiments CNTL30KM and CNTL3.3KM (times signs), between NNRPic and TOGAic (plus signs), between NNRPbc and TOGAbc (solid), between CNTL30KM and KFcps (circles), and between CNTL30KM and PERT30km (dashed). All experiments started at 0000 UTC 1 Jul 2002.

Experiment KFcps is performed in the same fashion as CNTL30KM except that the Kain and Fritsch (1990) cumulus parameterization scheme is used instead of the Grell (1993) scheme. Experiment GDmps is identical to CNTL30KM except that the Goddard microphysics parameterization scheme (Tao and Simpson 1993) is used instead of the Reisner et al. (1998) scheme. Experiment MRFpbl is the same as CNTL30KM except that the Medium-Range forecast (MRF) model boundary layer parameterization scheme (Hong and Pan 1996) is used instead of the Mellor and Yamada (1982) scheme. The 24-h accumulated precipitation from these sensitivity experiments is shown in Fig. 9. Not surprisingly, changes in various parameterizations produce great spread of forecasted accumulated precipitation. The largest difference from CNTL30KM comes from changing the cumulus parameterization scheme (Fig. 5a versus Fig. 9b), which is consistent with several previous studies (e.g., Wang and Seaman 1997; Gallus and Segal 2001). Moreover, the domain-integrated DTE between experiments with different cumulus schemes (CNTL30KM and KFcps) is comparable with that between experiments with different initial analyses (NNRPic and TOGAic) after only 3 h of integration (Fig. 8). The exact reasons for the divergence/discrepancies between these experiments are complex and beyond the scope of the current study. Each scheme will have a different impact on moist processes, especially the triggering of moist convection. As most of these parameterization schemes are still actively used in different NWP models, this forecast sensitivity can be regarded as a crude estimate of model

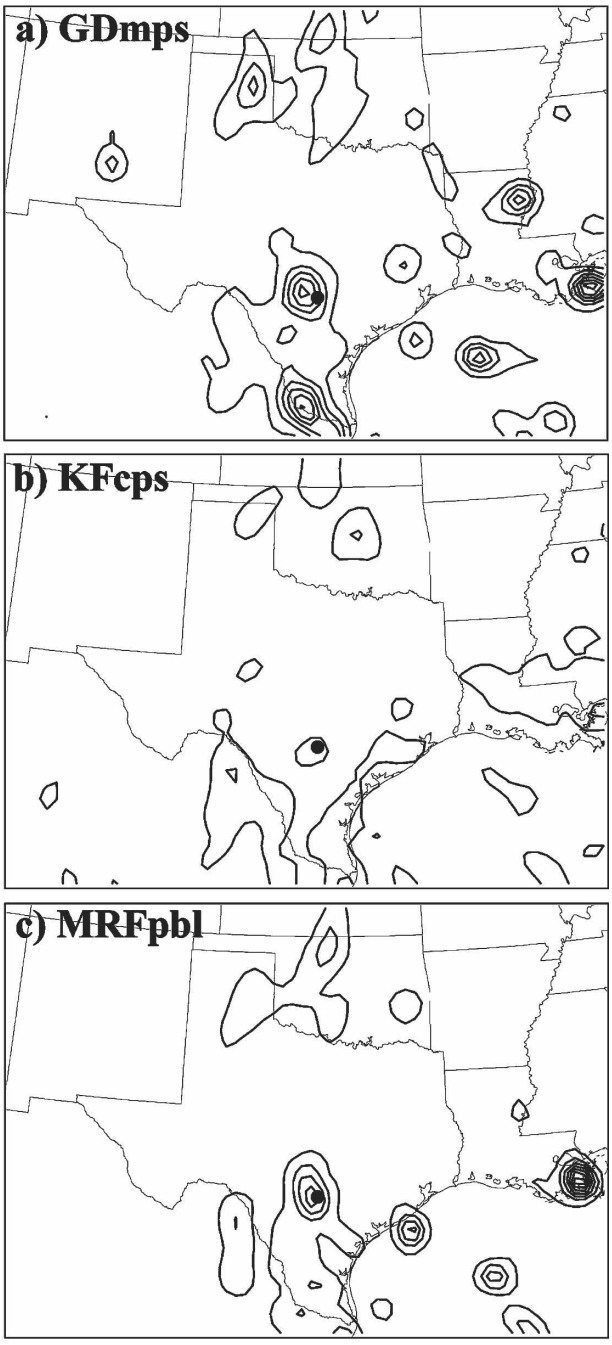

FIG. 9. The 24-h accumulated precipitation (every 20 mm) from 1200 UTC 1 Jul to 1200 UTC 2 Jul 2002 from experiments (a) GDmps, (b) KFcps, and (c) MRFpbl. All experiments started at 0000 UTC 1 Jul 2002.

error, which would obviously be detrimental to deterministic real-time forecasting for such severe warm-season events.

With advances in computational capability, NWP models are beginning to resolve some of the previously parameterized processes (e.g., moist convection) through higher and higher resolutions. In section 4a, we have demonstrated that increased resolution does not always deliver a better forecast. Moreover, there are still important physical processes, such as microphysics and boundary layer turbulence, which will need to be parameterized for the foreseeable future.

5. Intrinsic predictability

In sections 4b and 4c, we have demonstrated that realistic, large initial condition and model errors in current NWP systems can significantly limit the (practical) predictability of extreme weather like this flooding event. Further model development, more observations, and advances in data assimilation will likely lead to continuous reductions in both model errors and initial condition uncertainties, which should lead to better short-range mesoscale prediction. However, can we increase forecast accuracy indefinitely and how (intrinsically) predictable is the weather at mesoscales if the forecast model and initial conditions are *nearly* perfect? Consistent with the pioneering work of Lorenz (1969), ZSR03 demonstrated that, because of the chaotic nature of the atmosphere, very small initial errors in the forecast model can grow rapidly at small scales, quickly saturate, then spread upscale, substantially contaminating the 1–2-day mesoscale forecast for the January 2000 snowstorm. Moist convection and its consequences significantly limited intrinsic mesoscale predictability.

In this section, we will investigate the intrinsic predictability of this warm-season flooding event characterized by strong conditional instability but weak baroclinicity, in contrast to the midlatitude weather system with strong baroclinicity (ZSR03; Tan et al. 2004). Small errors in the initial conditions are unavoidable in any NWP systems because of the inherent uncertainties in observations and data assimilation methods. For simplicity, in this section, we assume the forecast model and the boundary conditions are perfect. In reality, as is true for initial conditions, there are also intrinsic uncertainties in any forecast model and its physical processes. In this case, the impact of boundary condition uncertainties is rather small, especially to the region of severe flooding.

a. Error growth in control simulations with parameterized convection

PERT30KM is identical to CNTL30KM, but with a perturbation added to the initial conditions. The perturbation consists of random, Gaussian noise added to the temperature field throughout the model domain ex-

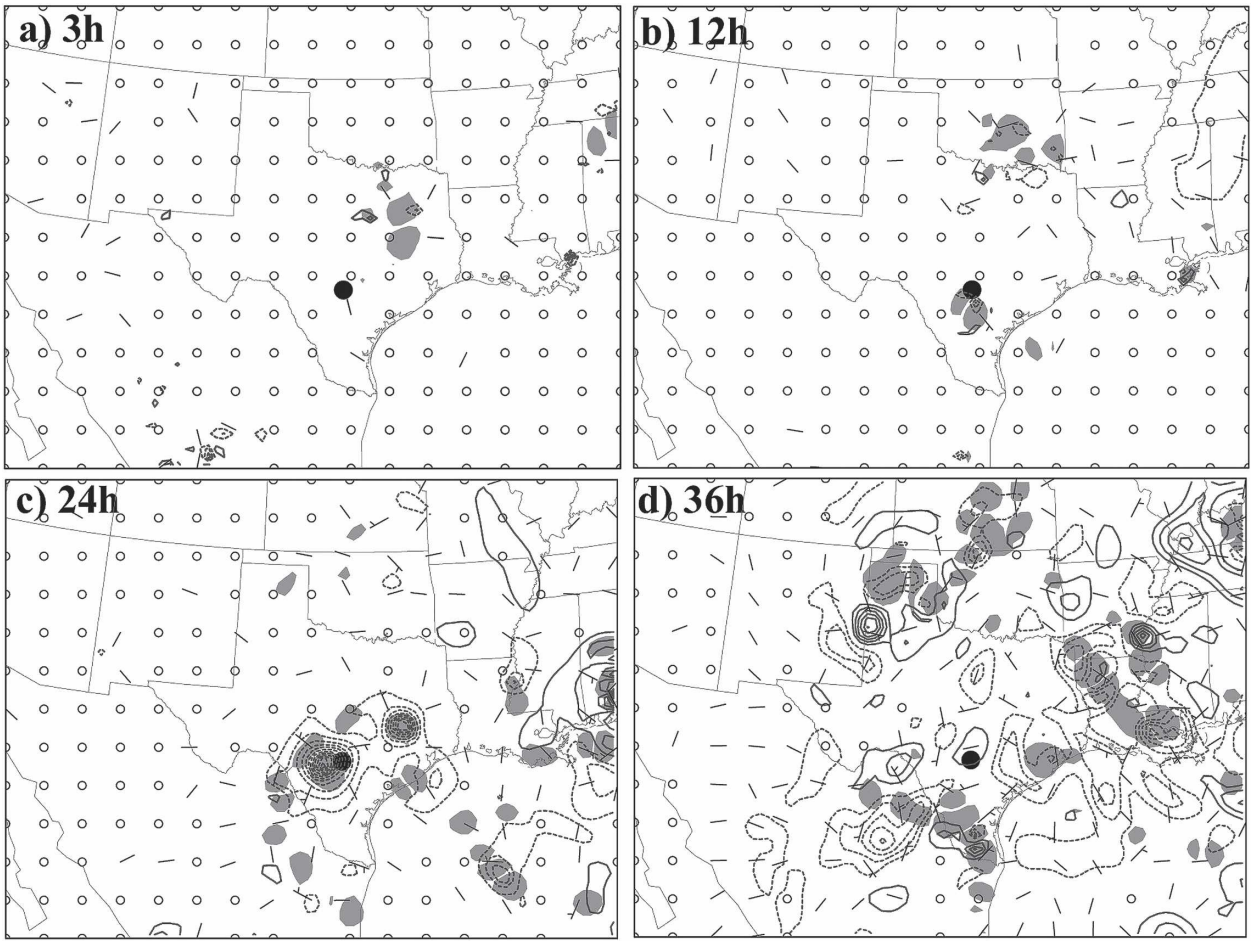

FIG. 10. The 500-hPa temperature (every 0.5 K; dashed, negative; solid, positive) and wind vector (full barb, 5 m s^{-1}) difference between CNTL30KM and PERT30KM valid at (a) 3-, (b) 12-, (c) 24-, and (d) 36-h forecast times. Areas with 3-h accumulated precipitation difference greater than 1 mm in CNTL30KM are shaded. Both experiments started at 0000 UTC 1 Jul 2002.

cept for the lateral boundaries; the noise has zero mean, standard deviation of 0.2 K, and is independent at each grid point and each grid level. Unlike the perturbation used in ZSR03, which was monochromatic with a wavelength of approximately 100 km, the perturbation used here follows Tan et al. (2004), which excites all horizontal scales.

Figure 10 shows the evolution of forecast temperature and wind difference at 500 hPa. After the first 3-h model integration (Fig. 10a), the initial random noise with standard deviation of 0.2 K subsided across the domain, except for some moderate growth in a few sporadic locations. Differences in wind vectors (~1 m s^{-1}), including those to the south of San Antonio, begin to emerge. The wind and temperature differences are often in similar places as precipitation differences (e.g., northeast Texas) where the 3-h accumulated precipitation differences are greater than 1 mm (shaded). At this time and earlier, the flow in the display domain is characterized by weak to moderate CAPE with little CIN (Fig. 11a), implying widespread moderate convective instability. At 12 h (Fig. 10b), coincident with precipitation differences, temperature and wind differences greater than 0.6 K and 2 m s^{-1} appear in the area south of San Antonio. In the meantime, wind and temperature differences are also found near the Texas–Oklahoma border and east of the Mississippi River. At 24 h (Fig. 10c), the maximum temperature difference has grown to 3–4 K in magnitude over a much larger area near and to the west of San Antonio. Organization of the wind difference in the same area is also apparent. There is convergence of wind vectors with cyclonic rotation toward the minimum temperature difference. Growth in the magnitudes of the wind and temperature difference fields, accompanied by precipitation difference, is seen in many places across most of the domain at 36 h (Fig. 10d). However, the difference near the San Antonio flooding area has weakened, likely due to the

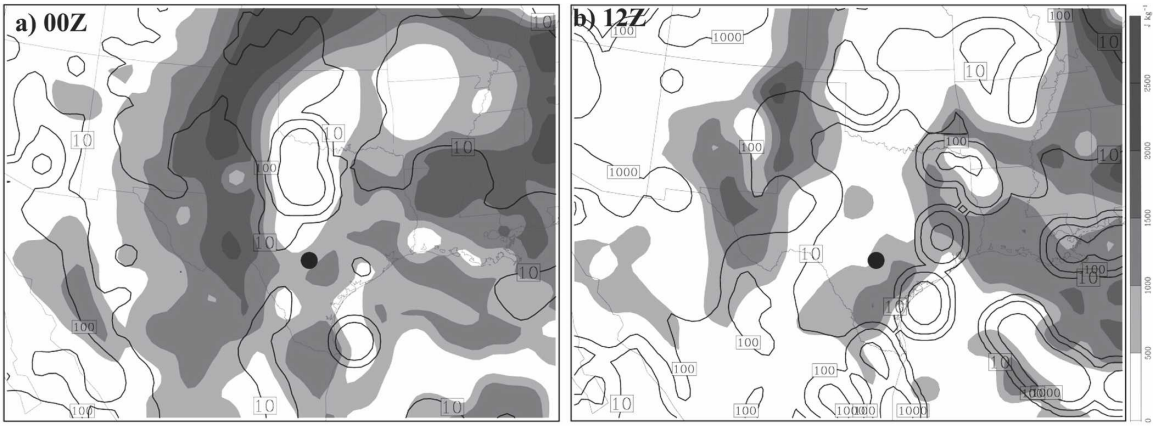

FIG. 11. Distribution of maximum CAPE (shaded every 500 J kg^{-1}) and CIN (only 10, 100, and 1000 J kg^{-1} are shaded) estimated from the CNTL30KM experiment valid at (a) 0000 and (b) 1200 UTC 1 Jul 2002.

cessation of precipitation in both the perturbed and unperturbed runs.

Further examination of the perturbed and unperturbed runs reveals that errors (difference) initially appear (0–3 h) at the convective scales (Fig. 10a), mostly in the area of moderate conditional instability (Fig. 11a) and in the presence of parameterized convection (similar to those in ZSR02). Parameterized convection also leads to larger but localized differences between the two model runs at later times (Figs. 10b–d). Evolution of the domain-integrated DTE (dotted curve in Fig. 8) also shows accelerated error growth between the 18- and 24-h forecast times, which corresponds well to the maximum daytime heating and reinvigorated convective instability (with CAPE–CIN patterns similar to Fig. 11a at 24 h). Domain-integrated DTE grows relatively slower at 12 h (early morning), possibly due to a small reduction in CAPE with larger areas of CIN in many parts of the domain (e.g., along the southern and eastern border regions of Texas in Fig. 11b). Figure 10 also indicates that the difference (error) is continuously expanding in areal coverage and growing in scale throughout the integration, but the upscale error growth is considerably weaker than the winter event of ZSR03 (their Fig. 2), which is further confirmed through the spectral analysis of the DTE shown in Fig. 12 (cf. to Fig. 3 of ZSR03).

The maximum difference of 24-h accumulated precipitation valid at 1200 UTC 2 July (with a 36-h lead time; Fig. 13a) is around 20%–30% of the forecast of total precipitation in CNTL30KM (Fig. 5a). The precipitation difference fields mostly appear in a quasi-dipole structure, indicating a displacement of local precipitation maxima between the two runs (e.g., convec-

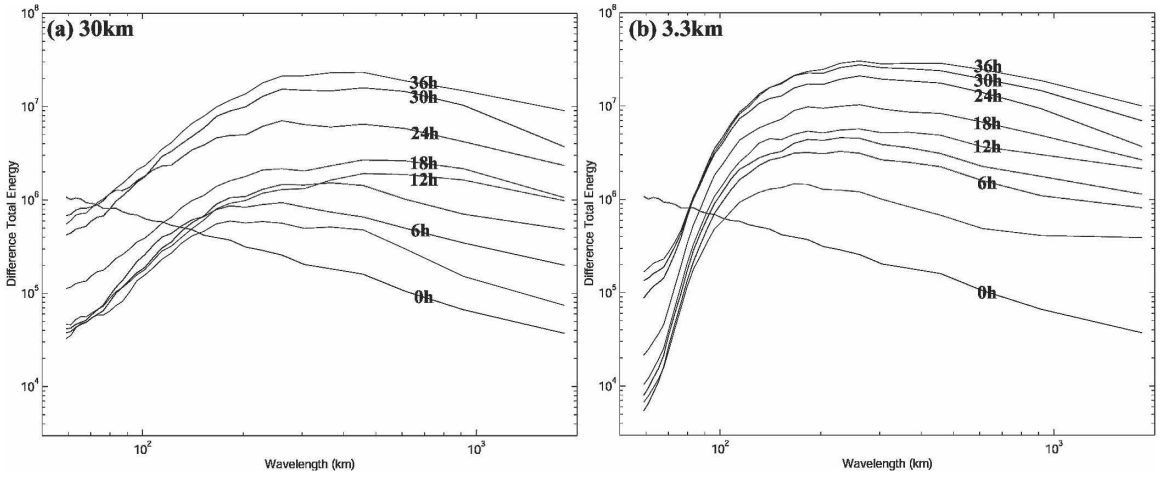

FIG. 12. Power spectra of the DTE ($m^2 s^{-2}$) between (a) CNTL30KM and PERT30KM and (b) CNTL3.3KM and PERT3.3KM. All simulations started at 0000 UTC 1 Jul 2002.

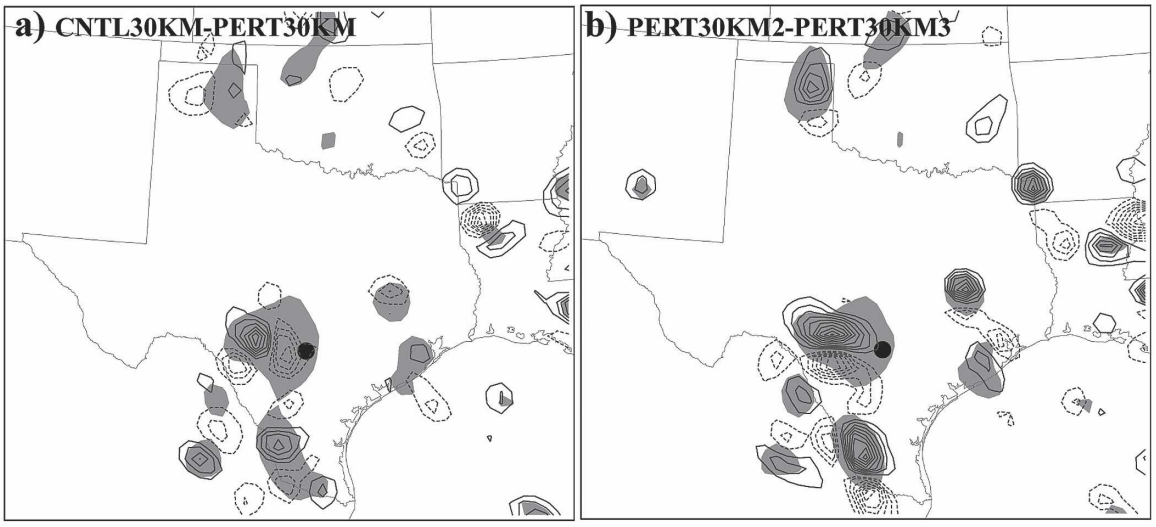

FIG. 13. (a) The 24-h accumulated precipitation difference (every 5 mm) between CNTL30KM and PERT30KM valid at the 36-h forecast time. (b) As in (a) but for the difference between PERT30KM2 and PERT30KM3. The 24-h accumulated precipitations greater than 20 mm in CNTL30KM and PERT30KM2 are shaded in (a) and (b), respectively. All simulations started at 0000 UTC 1 Jul 2002.

tive cells triggered in different locations but with similar strength). The same is true for the precipitation difference between two other perturbed runs with different realizations in initial random perturbations (Fig. 13b). The accumulated precipitation difference due to these small random perturbations is ~20% of the magnitude of those due to different initial analyses (Figs. 5a, 5c, and 5d). Thus, it is only of secondary importance (though not negligible) to the practical predictability issues, at least at the current time, when initial errors are still big and model errors are significant.

Experiments with five additional realizations of the initial perturbations are also performed. From examination of the evolution of the DTE between CNTL30KM and these five different realizations (Fig. 14a) and the wind and temperature difference fields (not shown), it is found that the error growth characteristics described above are quite generic. Moreover, similar error evolution is also found in an experiment with prescribed monochromatic small-scale and small-amplitude initial perturbation, as in ZSR03 (not shown).

In ZSR03, it is found that the smaller the initial difference, the faster the error growth. Similarly, we have performed several experiments configured exactly the same as PERT30KM but where the amplitudes of the random temperature perturbations are set to be 2.0, 0.2, 0.02, and 0.002 K, respectively. Consistent with ZSR03, the DTE evolution in Fig. 14b demonstrated that smaller-amplitude errors grow faster, indicating the mechanisms for error growth are also nonlinear. In terms of DTE, Fig. 14b also implies that, as the initial conditions become more accurate, a diminishing return in predictability will likely result due to the nonlinear error growth. For example, reducing the initial error by an order of magnitude from 0.2 to 0.02 K gains about 12 h of accuracy, while further reducing the error from 0.02 to 0.002 K gains only ~6–9 h.

Even though the error growth and upscale spreading are relatively weak, as in ZSR03, the rapid initial growth comes from parameterized moist processes, primarily due to the strong nonlinearity associated with conditional instability (refer to CAPE–CIN in Fig. 11). This is confirmed by the lack of error growth in the experiments similar to CNTL30KM and PERT30KM but with no latent heating feedback allowed ("fake dry"; Fig. 14c). In addition, we have performed several pairs of sensitivity experiments with the same initial conditions as CNTL30KM and PERT30KM but using the Kain–Fritsch cumulus parameterization scheme (i.e., KFcps), the Goddard microphysics scheme (i.e., GDmps), and the MRF boundary layer scheme (i.e., MRFpbl); the error growth characteristics are qualitatively similar to those between CNTL30KM and PERT30KM (Fig. 14c). As was also discussed in ZSR03, for the 30-km resolution, the nonlinearity is directly associated with the "on–off" switches, especially parameterized moist processes. Similar error growth occurs with any reasonable combination of parameterization schemes, as shown in Fig. 14c. As in ZSR03, if no cumulus parameterization is used, the nonlinearity will come from the "on–off" switches in

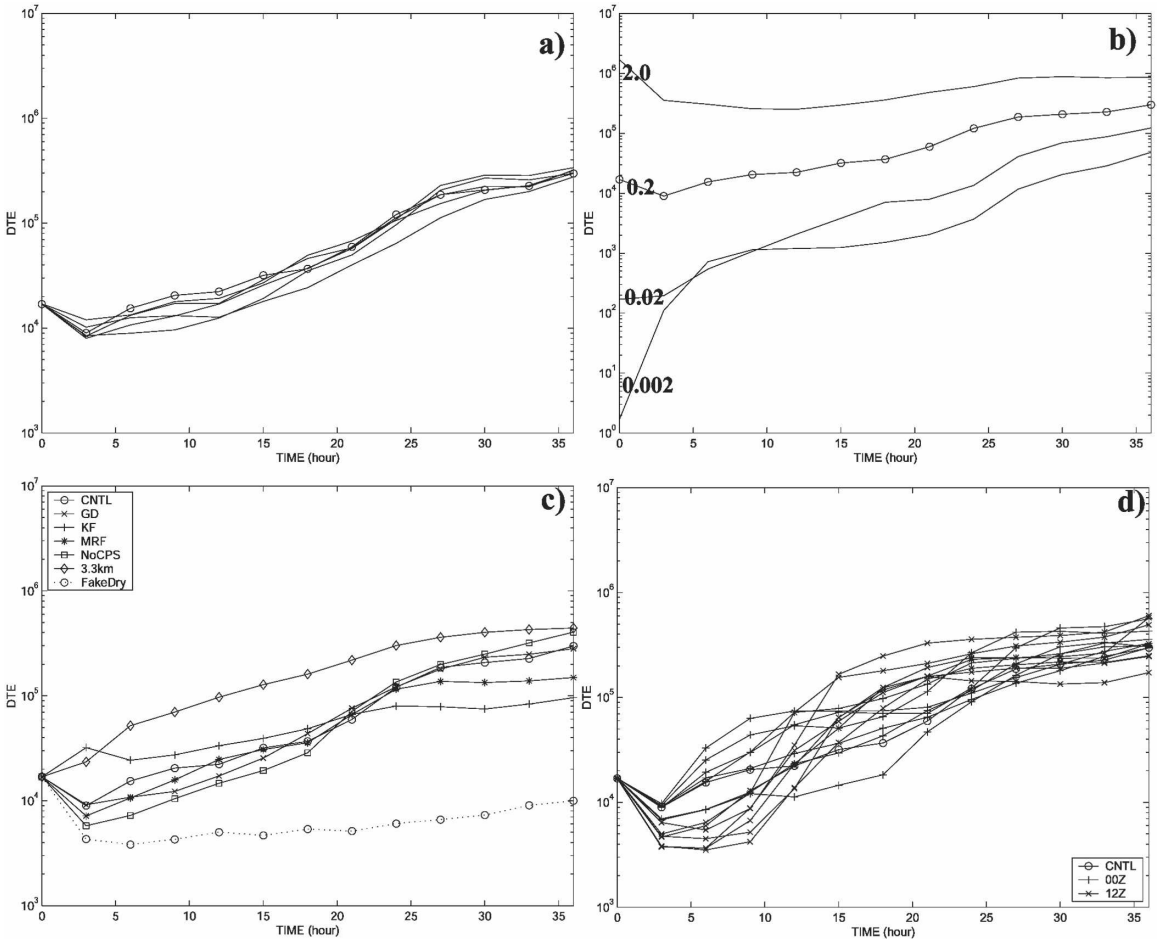

FIG. 14. Evolution of DTE ($m^2 s^{-2}$) (a) between CNTL30KM and experiments with different realizations of random perturbations; (b) between CNTL30KM and random perturbations with standard deviation of 0.002, 0.02, 0.2, and 2.0, respectively; (c) for experiments with different moist physics (details in text); and (d) between experiments similar to CNTL30KM and PERT30km but initialized at 15 different times (from 0000 UTC 28 Jun to 0000 UTC 5 Jul 2002, every 12 h). All experiments in (a)–(c) started at 0000 UTC 1 Jul 2002.

the microphysics parameterization schemes (NoCPS, Fig. 14c), though at a slightly later time. This is also true in the perturbed high-resolution experiments in which no CPS is needed (detailed in the next subsection) and in experiments initialized at different times during this multiday event (Fig. 14d, detailed in section 5c).

b. Error growth in high-resolution convective-resolving experiments

PERT3.3KM is identical to CNTL3.3KM (section 3) but with the same perturbed initial conditions as in PERT30KM for the 30-km coarse domain. The evolution of the forecast temperature and wind difference at 500 hPa is displayed in Fig. 15. Compared to the lower-resolution experiments with parameterized convection, the difference in the high-resolution experiments initially grows in similar places (except for the new local maximum in the Gulf of Mexico) but with significantly larger amplitude at 3 h (Fig. 15a versus Fig. 10a). Even though there is only a limited further increase in magnitude, the difference in all fields spreads to a much broader area at 12 and 24 h in the high-resolution runs (Figs. 15b and 15c versus Figs. 10b and 10c). At 36 h (Fig. 15d), there is still larger-scale organization of the difference fields. For example, the temperature in CNTL3.3KM is higher over a large region north and northwest of San Antonio than in PERT3.3KM while the wind difference displays a coherent cyclonic circulation, even though there is no significant precipitation in either of these two high-resolution runs in this region. The difference magnitudes of both winds and temperature are significantly smaller than those found between the two high-resolution experiments in

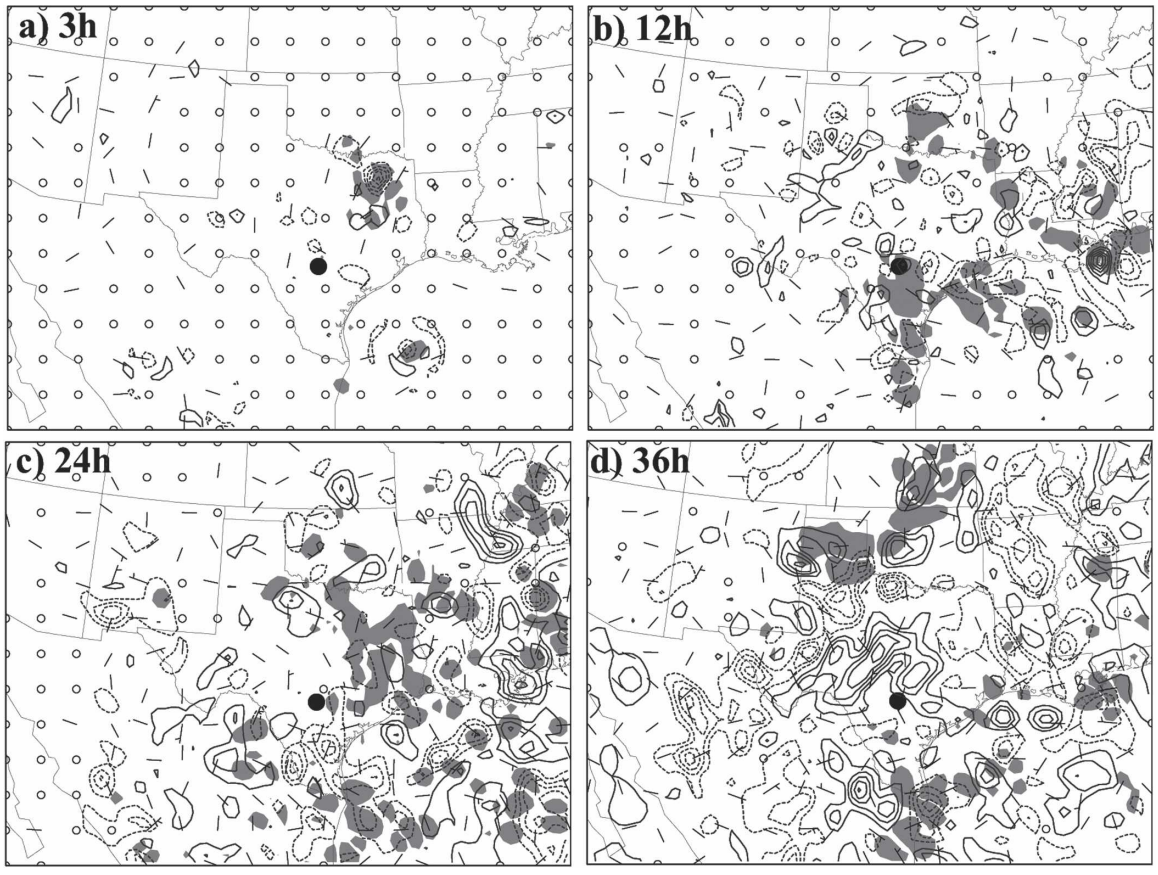

FIG. 15. The 500-hPa temperature (every 0.5 K; dashed, negative; solid, positive) and wind vector (full barb, 5 m s^{-1}) difference between CNTL3.3KM and PERT3.3km valid at (a) 3-, (b) 12-, (c) 24-, and (d) 36-h forecast times. Areas with 3-h accumulated precipitation difference greater than 1 mm in CNTL3.3KM are shaded.

ZSR03. Similarly, in the spectrum analyses of DTE between PERT3.3KM and CNTL3.3KM (Fig. 12b), even though the initial (0–6 h) error grows much faster than the lower-resolution runs at nearly all scales, there is no significant difference in the scale and amplitude of the DTE between the high- and low-resolution runs after 36 h of integration. The initial faster error growth coincides with a much larger area-averaged precipitation difference (and thus stronger difference in moist convection) in the high-resolution (3.3 km) simulations than in the 30-km simulations (refer to the dotted curves in Fig. 7). Consistently, the lack of error growth at later times may be due to the lack of precipitation in the high-resolution runs. A stronger upscale error growth is observed in the high-resolution experiments of ZSR03, in which stronger precipitation is simulated in high-resolution runs throughout the 36-h integration.

c. Error growth on different days; diurnal variation at 0000 and 1200 UTC

As discussed in section 2, this flooding event persisted for almost a week with few changes in synoptic-scale flow patterns, though there is strong variation of the attendant MCSs. As in Fig. 11, there are noticeable diurnal variations of larger-scale convective stability (some in CAPE but more so in CIN) over the entire period of the event. Similar to CNTL30KM and PERT30KM, we have performed 14 additional pairs of perturbed and unperturbed experiments every 12 h from 0000 UTC 28 June to 0000 UTC 4 July 2002, to examine the diurnal and daily variations of the error growth examined above. The evolution of DTE from all these pairs of experiments initiated at different times but with the same amplitude of initial random perturbations is displayed in Fig. 14d. The difference in DTE growth between pairs of experiment starting at 0000 UTC [marked with a plus sign (+)] and from the 1200 UTC (marked with an x) is obvious for the first 24-h integration. The initial (3–9 h) error growth from the 0000 UTC (early evening) runs is much faster that those from the 1200 UTC (early morning) runs because the flow is more convectively unstable in the late afternoon than in the early morning (refer to the CAPE and CIN plots in Fig. 11). But the error growth in the 1200 UTC

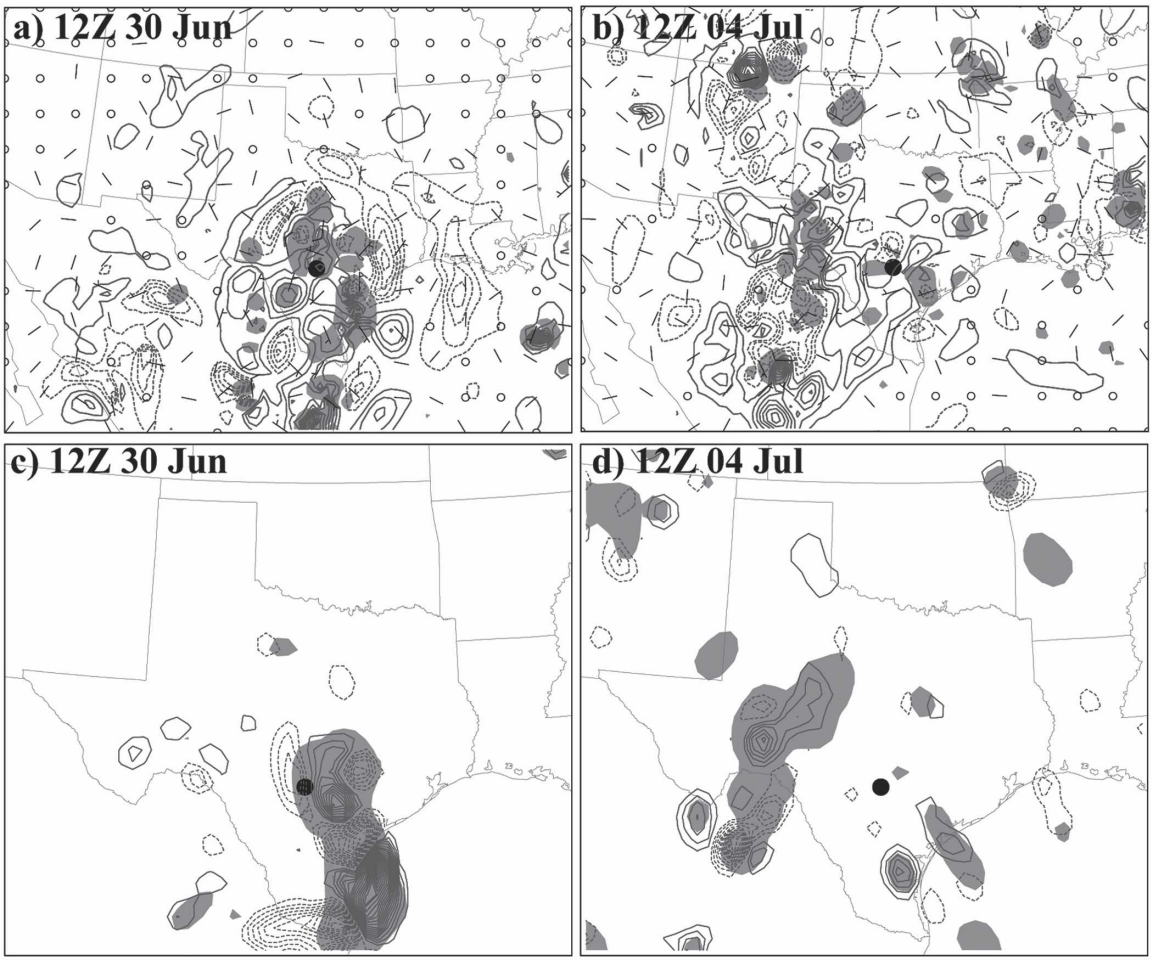

FIG. 16. (a), (b) As in Fig. 10d, but between experiments similar to CNTL30KM and PERT30km initialized at (a) 0000 UTC 29 Jun and (b) 0000 UTC 3 Jul 2002 [valid at (a) 1200 UTC 30 Jun and (b) 4 Jul 2002]. (c), (d) As in Fig. 13a but between experiments similar to CNTL30KM and PERT30km but initialized at (c) 0000 UTC 29 Jun and (d) 0000 UTC 3 Jul 2002 [valid at (c) 1200 UTC 30 Jun and (d) 4 Jul 2002].

runs catches up and even overtakes the others from between 12 and 21 h after these runs enter into the unstable stage. Despite strong variation in error growth rate during the first 24 h between experiments starting at different times, the DTEs from all runs approach similar amplitudes after 30 h.

We also examined the wind, temperature, and precipitation difference from these pairs of runs started at different times. Although the overall 36-h DTEs are similar between these pairs of experiments, the error growth is strongly flow dependent and variable dependent. For example, most of the 36-h forecast difference of the 500-hPa wind and temperature from the 0000 UTC 29 June runs is located at or east of San Antonio with a ~100 mm maximum in 24-h accumulated precipitation difference (Figs. 16a and 16c). However, the difference in the 0000 UTC 3 July runs is considerably weaker in amplitude and to the west of San Antonio (Figs. 16b and 16d). The localized error growth in both of these runs is consistent with the respective regions of convective activity (the shaded regions denote precipitation greater than 20 mm in their control runs; Figs. 16b and 16d).

6. Summary and discussion

This study uses the MM5 with grid spacings of 30 and 3.3 km to explore both the intrinsic and practical aspects of warm-season predictability, especially quantitative precipitation forecasts up to 36 h, with simulations of the 2002 San Antonio flooding event.

To study practical predictability, simulations were performed with various grid resolutions, initial and

boundary conditions, and physics parameterization schemes. It is found that the high-resolution convective-resolving simulation (with grid spacing down to 3.3 km) does not produce the best simulation or forecast. It was also found that, given the current analysis uncertainty, the initial analysis errors result in large forecast errors for this warm-season flooding event. The same is true for model errors as revealed by the substantial difference in forecasts through using different parameterizations schemes. Thus, practically, there is room to gain higher forecast accuracy through improving the initial analysis with better data assimilation techniques or enhanced observations, and through improving the forecast model with better-resolved or -parameterized physical processes.

For intrinsic predictability, even if a perfect forecast model is used, small-scale, small-amplitude initial errors, such as those in the form of undetectable random noise, can grow rapidly and, subsequently, contaminate the short-term deterministic mesoscale forecast within 36 h. The rapid error growth comes from moist convection. However, at present when the initial condition and model errors are still large, forecast errors arising from small-scale, small-amplitude random noise are found to be of secondary importance, though not negligible.

Our study further demonstrates the limited predictability for deterministic prediction of such a heavy precipitation event, both practically and intrinsically, and the need for probabilistic (ensemble) forecasts at the mesoscale. It also suggests that both initial condition and model uncertainties are important, and should be included in any ensemble forecast system. Intrinsic error growth and sensitivity to small perturbations will be inherently included in such probabilistic forecast systems.

It is also found that, compared with the cold-season mesoscale predictability studied in ZSR02 and ZSR03, the upscale spread of the error energy in the current warm-season flooding event seems to be weaker, and thus the impact to larger scales is relatively weaker. It is also found that, for the current event, small-scale small-amplitude errors in the high-resolution 3.3-km simulations grew faster than the lower-resolution 30-km, simulations only initially; they reached similar amplitudes and scales after 36 h. This is in strong contrast to ZSR03, in which error growth and upscale spread in terms of amplitude and scale are both stronger in the high-resolution 3.3-km simulations. The weaker upscale transfer of error energy in the current study may imply potentially longer intrinsic predictability for the warm-season atmosphere, which was also suggested by Reynolds et al. (1994) and Carbone et al. (2002).

The exact mechanisms for the differences between these two warm-season and cold-season extreme precipitation events are subject to future research. We noticed that, compared with the snowstorm of January 2000, the current warm-season flooding event has stronger convective instability but much weaker baroclinic instability. It is possible that convective instability determines error growth at smaller scales, while large-scale baroclinic (or barotropic) instability dictates upscale energy transfer and determines error growth at larger scales. More case studies are needed to test this hypothesis and to examine if these differences are general.

Acknowledgments. We thank the two anonymous reviewers for their valuable comments on an early version of the manuscript. Thanks are also due to Chris Snyder and Rich Rotunno for their comments on this subject. This research is supported by NSF Grant ATM-0205599 and by the Office of Navy Research under the Young Investigator Program (Award N000140410471).

REFERENCES

Caracena, F., and J. M. Fritsch, 1983: Focusing mechanisms in the Texas Hills County flash flood of 1978. *Mon. Wea. Rev.,* **111,** 2319–2332.

Carbone, R., J. D. Tuttle, D. A. Ahijevych, and S. B. Trier, 2002: Inferences of predictability associated with warm season precipitation episodes. *J. Atmos. Sci.,* **59,** 2033–2056.

Done, J., C. A. Davis, and M. Weisman, 2004: The next-generation of NWP: Explicit forecasts of convection using the Weather Research and Forecasting (WRF) model. *Atmos. Sci. Lett.,* **5,** 110–117.

Dudhia, J., 1993: A nonhydrostatic version of the Penn State–NCAR Mesoscale Model: Validation tests and simulation of an Atlantic cyclone and cold front. *Mon. Wea. Rev.,* **121,** 1493–1513.

Eckel, F. A., and C. F. Mass, 2005: Aspects of effective mesoscale, short-range ensemble forecasting. *Wea. Forecasting,* **20,** 328–350.

Ehrendorfer, M., 1997: Predicting the uncertainty of numerical weather forecast: A review. *Meteor. Z.,* **6,** 147–183.

Errico, R. M., R. Langland, and D. P. Baumhefner, 2002: The workshop in atmospheric predictability. *Bull. Amer. Meteor. Soc.,* **83,** 1341–1344.

Fowle, M. A., and P. J. Roebber, 2003: Short-range (0–48 h) numerical prediction of convective occurrence, mode, and location. *Wea. Forecasting,* **18,** 782–794.

Gallus, W. A., 2002: Impact of verification grid-box size on warm-season QPF skill measures. *Wea. Forecasting,* **17,** 1296–1302.

——, and M. Segal, 2001: Impact of improved initialization of mesoscale features on convective system rainfall in 10-km Eta simulations. *Wea. Forecasting,* **16,** 680–696.

Grell, G. A., 1993: Prognostic evaluation of assumptions used by cumulus parameterizations. *Mon. Wea. Rev.,* **121,** 764–787.

Grimit, E. P., and C. F. Mass, 2002: Initial results of a mesoscale short-range ensemble forecasting system over the Pacific Northwest. *Wea. Forecasting,* **17,** 192–205.

Hansen, J. A., 2002: Accounting for model error in ensemble-

based state estimation and forecasting. *Mon. Wea. Rev.,* **130,** 2373–2391.

Hong, S.-Y., and H.-L. Pan, 1996: Nonlocal boundary layer vertical diffusion in a medium-range forecast model. *Mon. Wea. Rev.,* **124,** 2322–2339.

Islam, S., R. L. Bras, and K. A. Emanuel, 1993: Predictability of mesoscale rainfalls in the Tropics. *J. Appl. Meteor.,* **32,** 297–310.

Kain, J. S., and J. M. Fristch, 1990: A one-dimensional entraining detraining plume model and its application in convective parameterization. *J. Atmos. Sci.,* **47,** 2784–2802.

Laprise, R., M. R. Varma, B. Denis, D. Caya, and I. Zawadzki, 2000: Predictability of a nested limited-area model. *Mon. Wea. Rev.,* **128,** 4149–4154.

Lorenz, E. N., 1963: The predictability of hydrodynamic flow. *Trans. New York Acad. Sci.,* **25B,** 409–432.

——, 1969: The predictability of a flow which possesses many scales of motion. *Tellus,* **21,** 289–307.

——, 1996: Predictability—A problem partly solved. *Proc. Seminar on Predictability,* Vol. I, Reading, United Kingdom, ECMWF, 1–19.

Mellor, G. L., and T. Yamada, 1982: Development of a turbulence closure model for geophysical fluid problems. *Rev. Geophys. Space Phys.,* **20,** 851–875.

Nielsen-Gammon, J. W., F. Zhang, A. Odins, and B. Myoung, 2006: Extreme rainfall events in Texas: Patterns and predictability. *Phys. Geogr.,* in press.

Odins, A. M., 2004: Mesoscale predictability of an extreme warm season precipitation event. M.S. thesis, Dept. of Atmospheric Sciences, Texas A&M University, 108 pp.

Olson, D. A., N. W. Junker, and B. Korty, 1995: Evaluation of 33 years of quantitative precipitation forecasting at the NMC. *Wea. Forecasting,* **10,** 498–511.

Reisner, J., R. J. Rasmussen, and R. T. Bruintjes, 1998: Explicit forecasting of supercooled liquid water in winter storms using MM5 Mesoscale Model. *Quart. J. Roy. Meteor. Soc.,* **124B,** 1071–1107.

Reynolds, C., P. J. Webster, and E. Kalnay, 1994: Random error growth in NMC's global forecast. *Mon. Wea. Rev.,* **122,** 1281–1305.

Snyder, C., and F. Zhang, 2003: Assimilation of simulated radar observations with an ensemble Kalman filter. *Mon. Wea. Rev.,* **131,** 1663–1677.

Stensrud, D. J., H. E. Brooks, J. Du, M. S. Tracton, and E. Rogers, 1999: Using ensembles for short-range forecasting. *Mon. Wea. Rev.,* **127,** 433–446.

Tan, Z., F. Zhang, R. Rotunno, and C. Snyder, 2004: Mesoscale predictability of moist baroclinic waves: Experiments with parameterized convection. *J. Atmos. Sci.,* **61,** 1794–1804.

Tao, W.-K., and J. Simpson, 1993: Goddard cumulus ensemble model. Part I: Model description. *Terr. Atmos. Oceanic Sci.,* **4,** 25–72.

Thompson, P. D., 1957: Uncertainty of initial state as a factor in the predictability of large scale atmospheric flow patterns. *Tellus,* **9,** 275–295.

Tracton, M. S., and E. Kalnay, 1993: Operational ensemble prediction at the National Meteorological Center: Practical aspects. *Wea. Forecasting,* **8,** 379–400.

Wang, W., and N. L. Seaman, 1997: A comparison study of convective parameterization schemes in a mesoscale model. *Mon. Wea. Rev.,* **125,** 252–278.

Warner, T. T., and H. M. Hsu, 2000: Nested-model simulation of moist convection: The impact of coarse-grid parameterized convection on fine-grid resolved convection. *Mon. Wea. Rev.,* **128,** 2211–2231.

——, R. A. Peterson, and R. E. Treadon, 1997: A tutorial on lateral boundary conditions as a basic and potentially serious limitation to regional numerical weather prediction. *Bull. Amer. Meteor. Soc.,* **78,** 2599–2617.

Zhang, F., 2005: Dynamics and structure of mesoscale error covariance of a winter cyclone estimated through short-range ensemble forecasts. *Mon. Wea. Rev.,* **133,** 2876–2893.

——, C. Snyder, and R. Rotunno, 2002: Mesoscale predictability of the "surprise" snowstorm of 24–25 January 2000. *Mon. Wea. Rev.,* **130,** 1617–1632.

——, ——, and ——, 2003: Effects of moist convection on mesoscale predictability. *J. Atmos. Sci.,* **60,** 1173–1185.

Zupanski, M., D. Zupanski, D. F. Parrish, E. Rogers, and G. DiMego, 2002: Four-dimensional variational data assimilation for the blizzard of 2000. *Mon. Wea. Rev.,* **130,** 1967–1988.